AN EXPLANATION FOR THE "SWITCH-ON" NATURE OF MAGNETIC ENERGY RELEASE AND ITS APPLICATION TO CORONAL HEATING

R. B. Dahlburg

Laboratory for Computational Physics and Fluid Dynamics, Naval Research Laboratory,
Washington, DC 20375-5344; rdahlbur@lcp.nrl.navy.mil

AND

J. A. Klimchuk and S. K. Antiochos

Space Science Division, Naval Research Laboratory, Washington, DC 20375

ABSTRACT

A large class of coronal heating theories postulate that the random mixing of magnetic footpoints by photospheric motions leads to the formation of current sheets in the corona and, consequently, to energy release there via magnetic reconnection. Parker pointed out that in order for this process to supply the observed energy flux into the corona, the stress in the coronal magnetic field must have a fairly specific value at the time that the energy is released. In particular, he argued that the misalignment between reconnecting flux tubes must be roughly 30° in order to match the observed heating. No physical origin for this number was given, however. In this paper we propose that secondary instability is the mechanism that "switches on" the energy release when the misalignment angle in the corona reaches the correct value. We calculate both the three-dimensional linear and fully nonlinear development of the instability in current sheets corresponding to various misalignment angles. We find that no secondary instability occurs for angles less than about 45°, but for larger angles the instability grows at a rapid rate, and there is an explosive release of energy. We compare our results with the observed properties of the corona and discuss the implications for future observations.

Subject headings: MHD — Sun: corona — Sun: magnetic fields

1. INTRODUCTION

There is widespread agreement that many coronal phenomena involve the release of free energy that is stored within stressed, current-carrying magnetic field configurations. Highly explosive events such as flares and coronal mass ejections are almost certainly explained in this way (Klimchuk 2001; Forbes 2002), and there is good reason to believe that less dramatic phenomena, such as the heating of coronal loops, also involve the conversion of magnetic energy (e.g., Mandrini et al. 2000). While an ample supply of magnetic free energy is clearly present in the corona, the process by which it is converted into heat and other forms remains a nagging unsolved problem. Any viable explanation must satisfy three conditions. The energy release mechanism must (1) remain dormant long enough for the magnetic stresses to build to the required levels, (2) proceed rapidly (at least as fast as the buildup rate) once it begins, and (3) convert enough of the available free energy to explain a particular phenomenon.

Energy release mechanisms that satisfy the second and third conditions have been known for some time, including Petschek-type magnetic reconnection, but they have not been demonstrated to have the "switch-on" property required by observations. In this paper we consider a promising mechanism called the secondary instability, which appears to satisfy all three conditions. This instability has been known for some time, but its tendency to activate only after magnetic stresses exceed a threshold has heretofore not been appreciated. As discussed in detail in earlier works (Dahlburg et al. 1992; Dahlburg 1997; Schumacher & Seehafer 2000; Dahlburg & Einaudi 2001, 2002), the energy release occurs at current sheets and proceeds in four stages: (1) the current sheet equilibrium is destabilized by a two-dimensional resistive instability (the primary instability);

(2) the resistive disturbance grows until it saturates nonlinearly to form a two-dimensional secondary equilibrium; (3) the two-dimensional equilibrium is itself destabilized by a three-dimensional ideal instability (the secondary instability); and (4) the three-dimensional disturbance grows to large amplitude and transitions to turbulence with enhanced energy dissipation. In this paper we show that the secondary instability occurs only in current sheets across which the magnetic field rotates by a sufficiently large angle. Thus, if the angle increases with time, as is the case when magnetic configurations are subjected to time-dependent shearing, the instability would switch on only after the critical angle is reached.

The importance of the switch-on nature of the energy release cannot be overstated. To illustrate this point, consider the well-known picture of coronal heating advocated by Parker (1983a, 1983b, 1988) and recently revisited by Priest et al. (2002). Parker proposed that random displacements of magnetic footpoints in the photosphere cause the coronal field to become wrapped and braided in complicated ways, perhaps resembling a bowl of tangled spaghetti. He further suggested that magnetic energy is released explosively as nanoflares at the interfaces between adjacent misaligned flux tubes. From global energy balance considerations, Parker estimated how large the angle of misalignment must become before a nanoflare occurs. Footpoint stressing motions pump energy into the coronal field at a rate given by the Poynting flux through the solar surface:

$$F = \frac{1}{4\pi} B_y B_x v_x, \qquad (1)$$

where B_y is the vertical component of the field and B_x is the horizontal component in the direction of motion, which has velocity v_x. By equating this flux with the combined radiation

losses from the corona and transition region (which is heated by downward thermal conduction from the corona) and by adopting typical observed values for B_y and v_x, Parker concluded that $B_x \approx 0.25B_y$ for a nanoflare to occur. This corresponds to a shear angle between adjacent flux tubes of $\theta = 2\arctan(0.25) \approx 30°$. For smaller angles, the Poynting flux would be inadequate to power the observed radiation losses, while for larger angles, the implied radiation would be too great.

We show here that the secondary instability has an angular dependence consistent with observations. Our approach involves a series of numerical MHD simulations of perturbed semi-infinite current sheet configurations. Each configuration has a fixed shear, or magnetic field rotation, but the shear varies from one configuration to the next. We find that weakly sheared configurations are stable, while strongly sheared configurations are unstable. Our preliminary results were presented in Dahlburg et al. (2003). The details of the numerical model are described in § 2, and the results of linear and nonlinear simulations are presented in §§ 3 and 4, respectively. The physical interpretation of the instability is discussed in greater detail in § 5. Section 6 is concerned with the thickness of coronal current sheets and is necessary for the discussion of coronal heating in § 7. The paper ends with a summary and final conclusions, as well as some discussion about future directions of this research.

2. NUMERICAL MODEL

We adopt the current sheet geometry that is shown schematically in Figure 1. The undisturbed background magnetic field has normalized shear ($\boldsymbol{B}_{0x}$) and guide ($\boldsymbol{B}_{0y}$) components given by

$$\boldsymbol{B}_{0x}(z) = C\tanh(z)\hat{\boldsymbol{e}}_x, \quad \boldsymbol{B}_{0y} = 1\hat{\boldsymbol{e}}_y, \tag{2}$$

where z is in units of the sheet half-width (l). The field rotates across the sheet by a total angle $\theta = 2\arctan(C)$. Thus, $C = \tan(\theta/2) = B_{0x}(z=\infty)/B_{0y}$ is a parameter that measures the shear. The initial velocity is taken to be zero. Note that the field is not force-free and so there is a mechanical pressure gradient given by the condition $dp/dz = \nabla \times \boldsymbol{B}_0 \times \boldsymbol{B}_0$. This simplified one-dimensional field, with quantities varying only in the z-direction, is meant to represent a subregion within a much larger three-dimensional configuration (e.g., a "patch" at the interface between two misaligned coronal flux tubes). Readers should not misconstrue θ as the pitch angle of the magnetic field within a twisted flux tube.

We solve numerically the dissipative, incompressible MHD equations, written in a dimensionless rotation form:

$$\frac{\partial \boldsymbol{v}}{\partial t} = \boldsymbol{v} \times \boldsymbol{\zeta} - \nabla\Pi + \boldsymbol{j} \times \boldsymbol{B} + \frac{1}{S_v}\nabla^2\boldsymbol{v}, \tag{3a}$$

$$\nabla \cdot \boldsymbol{v} = 0, \tag{3b}$$

$$\frac{\partial \boldsymbol{B}}{\partial t} = \nabla \times \boldsymbol{v} \times \boldsymbol{B} - \frac{1}{S}\nabla \times \boldsymbol{j}, \tag{3c}$$

$$\nabla \cdot \boldsymbol{B} = 0, \tag{3d}$$

where $\boldsymbol{v}(\boldsymbol{x}, t)$ is the flow velocity, $\boldsymbol{\zeta}(\boldsymbol{x}, t) = \nabla \times \boldsymbol{v}$ is the vorticity, $\boldsymbol{B}(\boldsymbol{x}, t)$ is the magnetic field, $\boldsymbol{j}(\boldsymbol{x}, t) = \nabla \times \boldsymbol{B}$ is the electric current density, $\Pi(\boldsymbol{x}, t)$ is the mechanical pressure plus kinetic energy density, S is the Lundquist number, and S_v is the viscous Lundquist number. The resistivity and viscosity are assumed to be constant and uniform. We measure distance in units of the current sheet half-width (l), magnetic field in units of the guide field (B_{0y}), velocity in units of the Alfvén speed (V_A), and time in units of the Alfvén transit time across the sheet
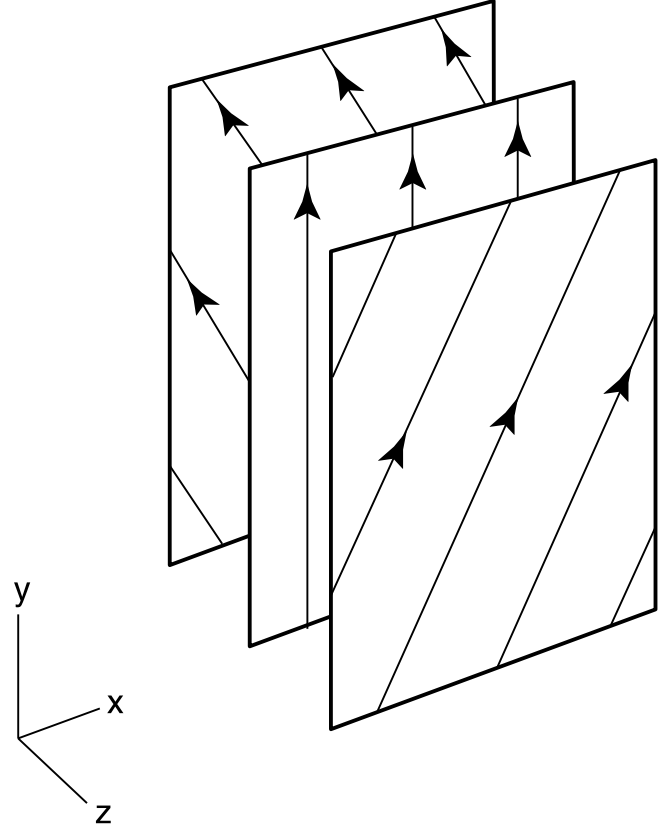

FIG. 1.—Definition sketch of the sheared magnetic field.

($\tau_A = l/V_A$). The simulations are carried out with our three-dimensional Fourier pseudospectral–Fourier collocation code (Dahlburg et al. 1992) in which the magnetic and velocity fields are expanded in the form

$$\boldsymbol{B}(x, y, z, t) = \sum_{|m|\leq M/2}\sum_{|n|\leq N/2}\sum_{p=0}^{P}\tilde{\boldsymbol{B}}(m, n, p, t)e^{i(m\alpha x + n\beta y)}f_i(Z), \tag{4a}$$

$$\boldsymbol{v}(x, y, z, t) = \sum_{|m|\leq M/2}\sum_{|n|\leq N/2}\sum_{p=0}^{P}\tilde{\boldsymbol{v}}(m, n, p, t)e^{i(m\alpha x + n\beta y)}f_i(Z), \tag{4b}$$

$$f_i(Z) = \begin{cases} \cos(pZ), & i = x, y, \\ \sin(pZ), & i = z, \end{cases} \tag{4c}$$

and i denotes the three Cartesian directions. The spatial variable Z is a transformation of z such that $-\infty \leq z \leq \infty$ maps onto $-1 \leq Z \leq 1$. The smallest wavenumbers (longest wavelengths) treated in our system are α in the x-direction and β in the y-direction. Thus, the simulation box has the effective dimensions $0 \leq x \leq 2\pi/\alpha$, $0 \leq y \leq 2\pi/\beta$, and $-L_z \leq z \leq L_z$. Periodic boundary conditions are imposed in the x- and y-directions and free-slip boundary conditions in the z-direction.

As described above, the energy release we are studying involves four distinct stages, beginning with the linear growth of the primary instability and ending with a nonlinear transition to turbulence of the secondary instability. Treating all four stages with a single do-it-all simulation is not numerically

feasible. We therefore begin each simulation near the end of the first stage, when the primary instability is close to saturation. We approximate this state by modifying the initial equilibrium of equation (2) with a large-amplitude dose of its fastest growing unstable eigenmode. Earlier studies have shown this to be a long-wavelength two-dimensional mode with wavenumber $k_x \approx 0.2$ (Dahlburg et al. 1986; Dahlburg & Karpen 1995; Seehafer & Schumacher 1998). Essentially, it consists of a series of straight infinite flux tubes lined up side by side along the current sheet and directed parallel to the y-axis. When viewed in cross section, the tubes produce the familiar chain of resistive tearing islands. By choosing $\alpha = 0.2$, we associate this most unstable eigenmode with the $(m, n) = (1, 0)$ mode in our expansion in equations (4a) and (4b). The spatial dependence $f_i(Z)$ is simply the eigenfunction obtained by solving the linearized eigenvalue problem using a Chebyshev-τ technique (Dahlburg et al. 1983).

To initiate the secondary instability, which has important structure in the y-direction, we further modify the equilibrium with a small-amplitude dose of its $(m, n) = (1, 1)$ eigenmode. Although three-dimensional modes (defined as modes with $n \neq 0$) grow slowly in the original equilibrium, they grow rapidly in the new equilibrium that is formed when the primary instability saturates. The initial magnetic and velocity fields of our simulations are thus given by

$$\boldsymbol{B}(x, y, z, t=0) = \boldsymbol{B}_0(z) + \epsilon_{2D}\boldsymbol{B}_{2D}(z)e^{i\alpha x}$$
$$+ \epsilon_{3D}\boldsymbol{B}_{3D}(z)e^{i(\alpha x + \phi) + i\beta y}, \quad (5a)$$

$$\boldsymbol{v}(x, y, z, t=0) = \epsilon_{2D}\boldsymbol{v}_{2D}(z)e^{i\alpha x} + \epsilon_{3D}\boldsymbol{v}_{3D}(z)e^{i(\alpha x + \phi) + i\beta y},$$
$$(5b)$$

where $\boldsymbol{B}_0(z)$ is the unperturbed background field, $\boldsymbol{B}_{2D}$ and $\boldsymbol{v}_{2D}$ are from the $(1, 0)$ eigenmode, and $\boldsymbol{B}_{3D}$ and $\boldsymbol{v}_{3D}$ are from the $(1, 1)$ eigenmode. We impose a phase shift $\phi = \pi/2$ between the eigenmodes. The primary instability is known to saturate at an amplitude of approximately 0.01 (see Dahlburg 1994, 1998), and we therefore choose a somewhat smaller initial amplitude of $\epsilon_{2D} = 0.002$ or 0.003, depending on the run. This amplitude refers to the x-component of the perturbed magnetic field, normalized to the background, B_{0y}. The y- and z-components and all components of the perturbed velocity are scaled accordingly. We use different initial amplitudes for the three-dimensional eigenmode. For the linear simulations, we begin with an extremely small perturbation $\epsilon_{3D} = 10^{-14}$, and for the nonlinear simulations, we begin with a larger but still small $\epsilon_{3D} = 5 \times 10^{-6}$ or 10^{-3}, again depending on the run. Table 1 indicates the

TABLE 1
Simulation Parameters

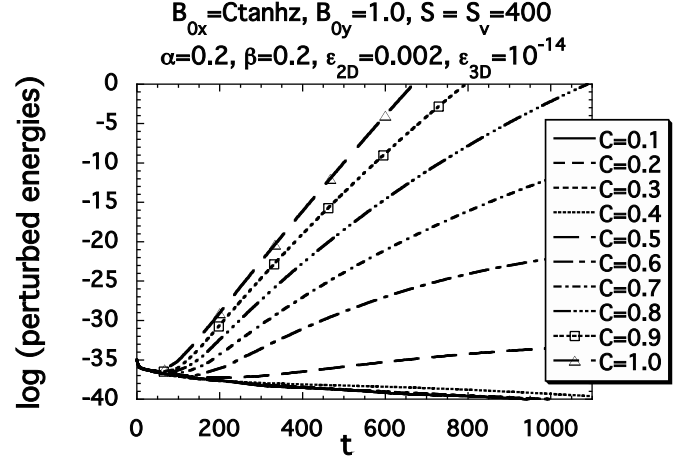| Figure	ϵ_{2D}	ϵ_{3D}	$S = S_V$
2	0.002	10^{-14}	400
3	0.002	10^{-14}	400
4	0.002	10^{-14}	400
5	0.003	5×10^{-6}	400
6	0.003	5×10^{-6}	400
7	0.003	5×10^{-6}	200
8	0.002	10^{-3}	1000
9	0.002	10^{-3}	1000
10	0.002	10^{-14}	400
11	0.002	10^{-14}	400

Fig. 2.—Three-dimensional linear perturbed energy as a function of time parameterized by the shear parameter (C) for a case with equal fieldwise and sheetwise wavenumbers.

parameter values used for the simulations shown in the figures. In all cases, $\alpha = 0.2$ and $L_z = 250$; $\beta = 0.2$ except in Figures 3 and 4.

3. LINEAR GROWTH OF THE SECONDARY INSTABILITY

To follow the linear development of the secondary instability, it is sufficient to truncate our expansion in equations (4a) and (4b) at $N = 2$, $M = 16$, and $P = 16$. We consider a series of runs in which C varies between 0.1 and 1.0. As a measure of the growth of the instability, we compute the energies in the different modes by integrating over the computational box:

$$E_{mn}(t) = \frac{\pi^2}{2\alpha\beta} \int_{-L_z}^{L_z} \left[|\boldsymbol{B}_{mn}(z, t)|^2 + |\boldsymbol{v}_{mn}(z, t)|^2 \right] dz, \quad (6)$$

where

$$\boldsymbol{B}_{mn}(z, t) = \sum_{p=0}^{P} \tilde{\boldsymbol{B}}(m, n, p, t)f_i(Z), \quad (7a)$$

$$\boldsymbol{v}_{mn}(z, t) = \sum_{p=0}^{P} \tilde{\boldsymbol{v}}(m, n, p, t)f_i(Z). \quad (7b)$$

The energy of the secondary instability is then determined by summing over the three-dimensional modes with $n = 1$:

$$E_{3D}(t) = \sum_m E_{m,1}(t). \quad (8)$$

Higher order three-dimensional modes are not significant in the linear regime. The evolution of E_{3D} is illustrated in Figure 2. We see that the energy grows with time only for $C > 0.4$. Thus, for these model parameters, the secondary instability is linearly unstable only when the shear angle exceeds $\theta \approx 2 \arctan(0.4) = 44°$. The growth times in Figure 2 range from $68\tau_A$ for $C = 0.5$ down to $6.6\tau_A$ for $C = 1.0$. Since $\tau_A \sim 0.1$ s (see below), the instability is very fast. The deviation from a pure exponential (straight line) for the unstable C and the slow energy decay for the stable C are due to ohmic and viscous dissipation.

Our choice $\beta = 0.2$ is somewhat arbitrary, so to determine whether the choice is important, we consider a second set of simulations using $\beta = 0.1$. The evolution of E_{3D} is shown in
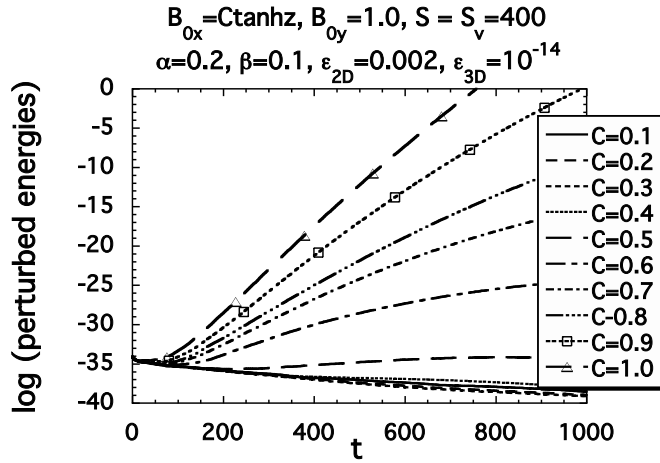
FIG. 3.—Three-dimensional linear perturbed energy as a function of time parameterized by the shear parameter (C) for a case with unequal fieldwise and sheetwise wavenumbers.

FIG. 4.—Dispersion relation of the secondary mode with respect to the sheetwise wavenumber β.

Figure 3. The behavior is qualitatively very similar to the $\beta = 0.2$ case, although there are some minor differences. The growth times are slightly longer, but, as before, instability first occurs when C exceeds 0.4.

To further investigate the dependence on β, we performed several runs at $C = 1.0$ with different values of β and several values of the Lundquist numbers. Growth rates of E_{3D} are plotted as a function of β in Figure 4. They peak near $\beta = 0.5$ but are not appreciably different at 0.2, the value used for most of our runs. We also see that the growth rate increases with Lundquist number for our runs. We believe this is due, in part, to the fact that the basic x-magnetic field (initially equal to $\tanh z$) decays at a rate dependent on S during the time in which the primary instability grows and eventually attains finite amplitude. Thus, when the secondary instability begins to grow, the basic magnetic field is different for different values of S and S_V. In addition, the secondary instability may itself be weakly dependent on the resistivity.

4. NONLINEAR EVOLUTION OF THE SECONDARY INSTABILITY

To investigate whether the secondary instability grows to sufficient amplitude to be energetically important requires a nonlinear treatment. This necessitates the inclusion of many more modes in the expansion in equations (4a) and (4b). We use $N = M = P = 128$. Because of the extra computational demands that this imposes, we start each simulation with a much larger three-dimensional perturbation of $\epsilon_{3D} = 5 \times 10^{-6}$.

Figure 5 shows the evolution of several individual modes for cases of weak ($C = 0.1$) and strong ($C = 1.0$) shear. Plotted are the volume integrals of the magnetic energies of each of the modes. Recall that we initialize each simulation with a modest dose of the (1, 0) eigenmode, to place the system close to the nonlinear saturation of the primary two-dimensional resistive instability, as well as a small dose of the (1, 1) eigenmode, to initiate three-dimensional evolution. These modes therefore have finite amplitude at $t = 0$ in the figures. Let us first consider the case of weak shear (Fig. 5, left). The initial two-dimensional perturbation grows until saturation at about $t = 250$. As it does, it excites higher order two-dimensional modes, which are also resistively unstable and saturate at roughly the same time. Thereafter, all the modes decay slowly because of ohmic and viscous dissipation. The imposed three-dimensional perturba-
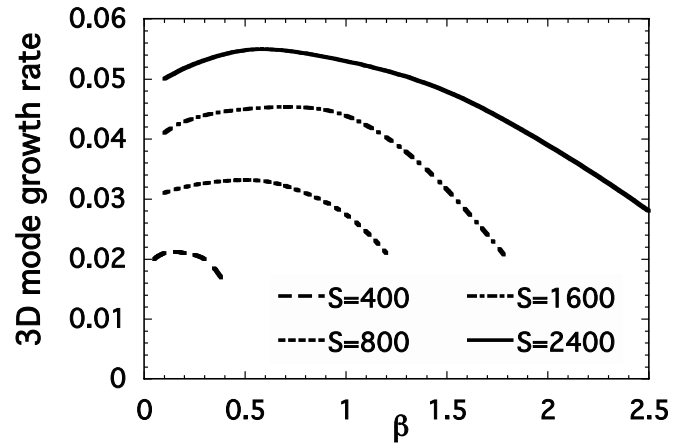
tion decays from the very start, as expected from our linear results.

The two-dimensional modes evolve very similarly in the case of strong shear (Fig. 5, right). They saturate at a higher level because there is 100 times more energy in the shear component of the background field ($C^2 = 1.0$ vs. 0.01). The three-dimensional modes exhibit a dramatically different behavior, on the other hand. They decay initially because of ohmic and viscous effects, but then they undergo rapid growth as the primary instability saturates and the secondary instability takes off. This is striking evidence of how the primary instability creates the conditions that are necessary for the secondary instability to occur. The three-dimensional modes finally saturate at about $t = 1000$ after increasing by many orders of magnitude.

Figure 6 (left) shows the evolution of the kinetic energies (not magnetic, as in Fig. 5) of the individual modes for the strong-shear case. In the late stages, all the two-dimensional modes have considerably smaller energy than the three-dimensional modes. This indicates a cascade of energy toward larger wavenumbers (shorter wavelengths), suggestive of turbulence. The cascade is more clearly evident in Figure 6 (right), which shows the average kinetic energy wavenumber as a function of time for both the weak and strong-shear cases. We obtain this wavenumber simply by computing the square root of the ratio of the enstrophy to the kinetic energy (e.g., Horiuchi & Sato 1986). For the weak-shear case, not much change is observed, implying the absence of spectral transfer. For the strong-shear case, however, a significant increase in this variable is seen as the system becomes nonlinear. The increase in magnitude implies the existence of a direct cascade of energy.

Several important features relating to the development of the secondary instability are portrayed in Figure 7, which shows isosurfaces of the electric current magnitude ($j = |\nabla \times \boldsymbol{B}|$) well into the nonlinear regime. Note that the orientation is rotated by $90°$ compared to Figure 1. Figure 7a shows the basically two-dimensional filamentation of the current that occurs as the primary resistive instability saturates to form a secondary equilibrium. The secondary instability initially appears at this time as a slight bending and twisting of the filament, but by the time of Figure 7b it has completely overwhelmed the two-dimensional state, and the current structure assumes a purely three-dimensional form. It resembles what might be called a "twisted double fishtail." (Recall that the system is periodic in x and y, so the two "fishtails" are actually connected.) This configuration differs significantly from the serpentine shape seen in simulations with
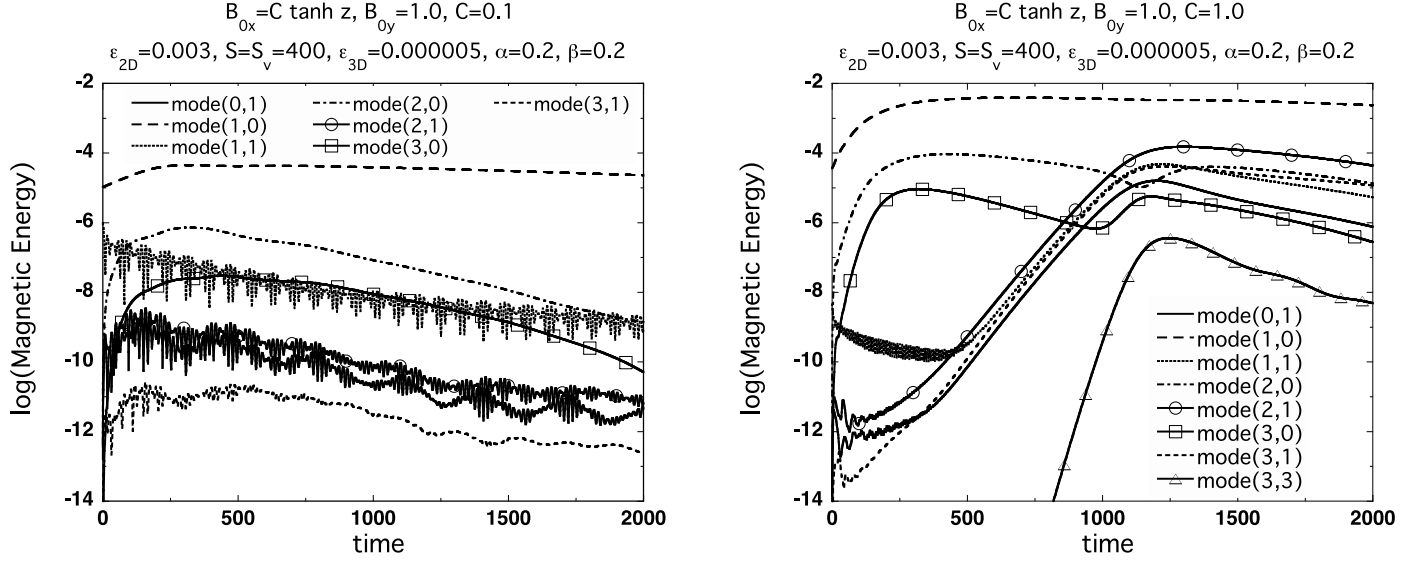
Fig. 5.—*Left*, Magnetic energy harmonic history for a low-shear case ($C = 0.1$); *right*, magnetic energy harmonic history for a high-shear case ($C = 1.0$).

no guide field (Dahlburg et al. 1992; Dahlburg & Einaudi 2002). The fishtail structure is disrupted by the time of Figure 7c, and the currents assume an arguably turbulent appearance. At late times the system settles down to the state shown in Figure 7d.

The concentration of the electric current on small scales intensifies the current density and an associated increase in ohmic dissipation. In addition, there is enhanced viscous dissipation due to the complicated flow patterns that develop with regions of large vorticity. Both effects lead to plasma heating. The total heating rate integrated over the computational box is given by

$$Q = \frac{J}{S} + \frac{\Omega}{S_v}, \qquad (9)$$

where S is the Lundquist number, S_v is the viscous Lundquist number, Ω is the integrated square of the vorticity (enstrophy),

$$\Omega = \int_{-L_z}^{L_z} \int_0^{2\pi/\beta} \int_0^{2\pi/\alpha} |\nabla \times \boldsymbol{v}|^2 \, dx \, dy \, dz, \qquad (10a)$$

and J is the integrated square of the electric current density,

$$J = \int_{-L_z}^{L_z} \int_0^{2\pi/\beta} \int_0^{2\pi/\alpha} |\nabla \times \boldsymbol{B}_p|^2 \, dx \, dy \, dz. \qquad (10b)$$

Here, $\boldsymbol{B}_p$ is the perturbed magnetic field, defined as

$$\boldsymbol{B}_p = (b_x, \ b_y, \ b_z), \qquad (11)$$

with

$$b_i(x, \ y, \ z, \ t) = B_i(x, \ y, \ z, \ t) - \overline{B}_i(z, \ t), \qquad (12)$$

$$\overline{B}_i(z, \ t) = \frac{\alpha\beta}{4\pi^2} \int_0^{2\pi/\beta} \int_0^{2\pi/\alpha} B_i \, dx \, dy, \qquad (13)$$

where B_i denotes either B_x, B_y, or B_z. We use the perturbed magnetic field rather than the total magnetic field because of the artificially large electrical resistivity and correspondingly small magnetic Lundquist number in our simulations. In the
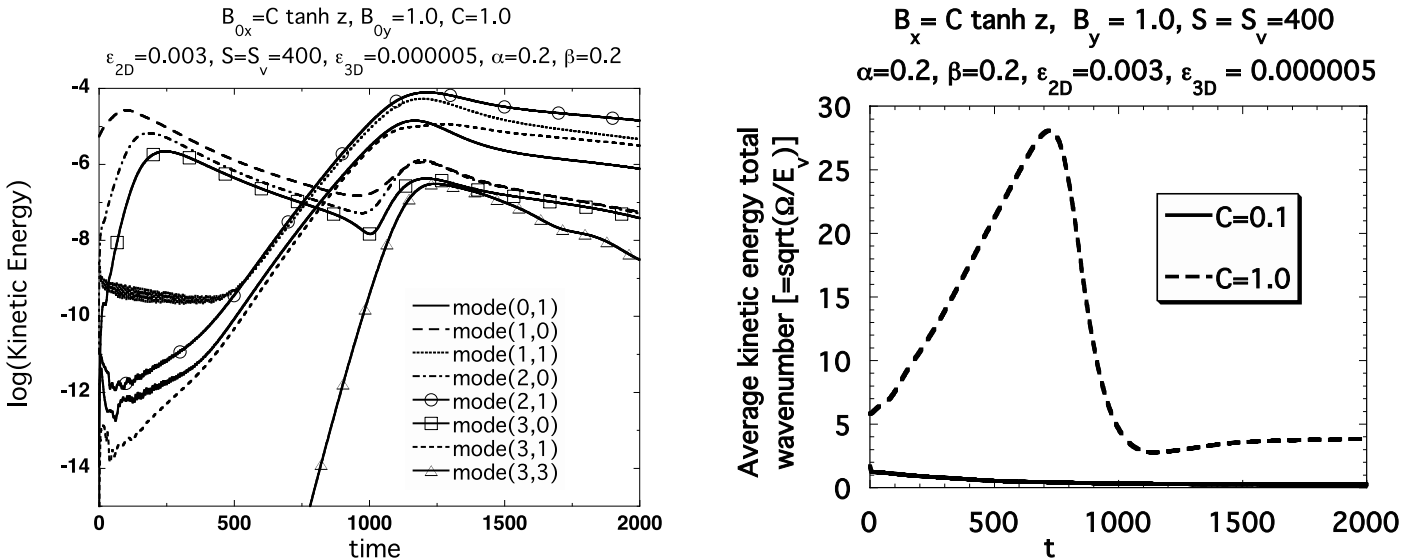

Fig. 6.—*Left*, Kinetic energy harmonic history for a high-shear case ($C = 1.0$); *right*, average kinetic energy total wavenumber as a function of time for a high-shear case ($C = 1.0$).
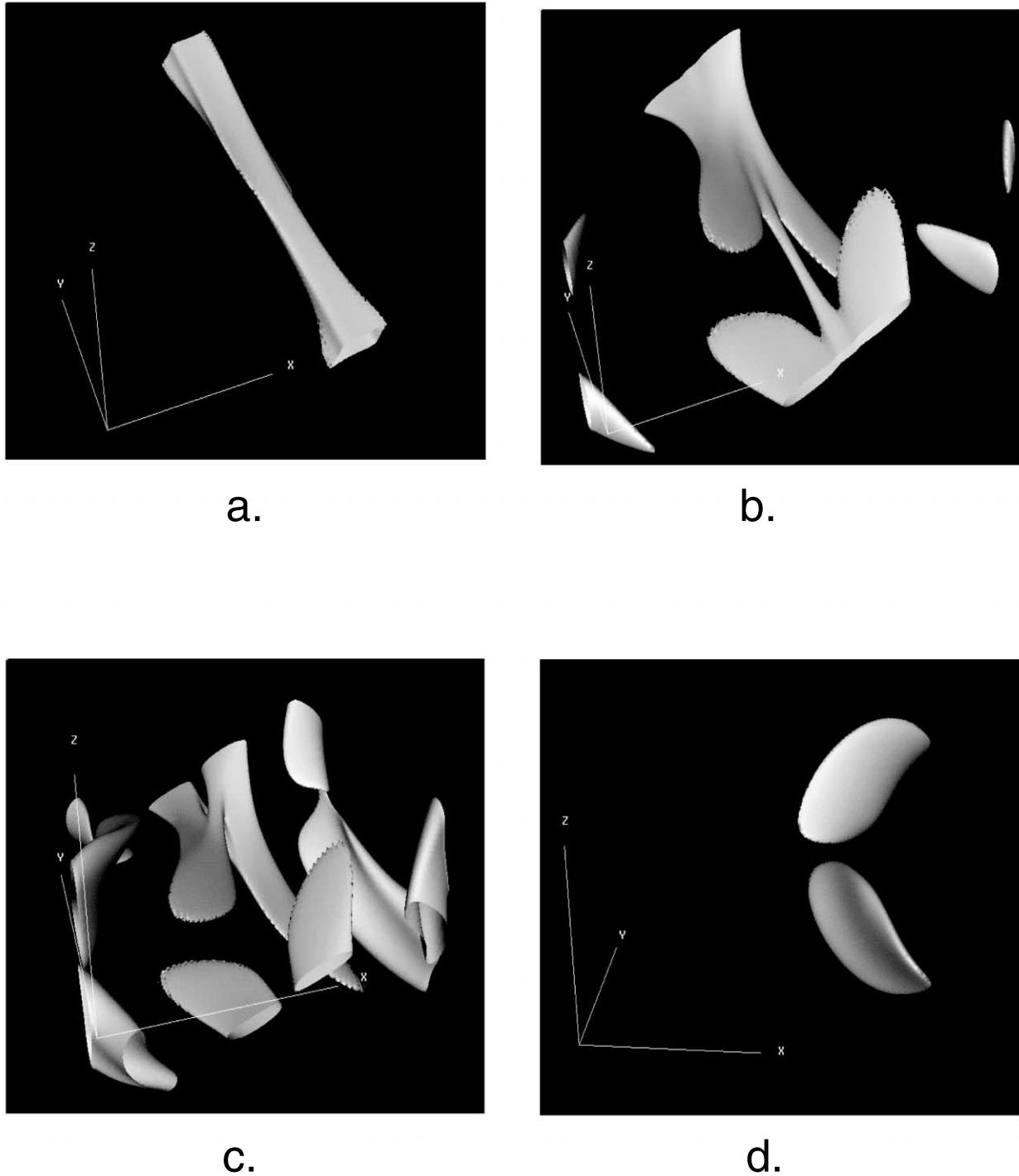
Fig. 7.—Isosurfaces of electric current magnitude j at four times during the three-dimensional evolution for $C = 1.0$ and $S = S_v = 200$. The times and isosurface values are (a) $t = 177.84$, $j = 0.5814$; (b) $t = 244.53$, $j = 0.4478$; (c) $t = 266.76$, $j = 0.4236$; and (d) $t = 288.99$, $j = 0.6017$. In (d) the data have been shifted by a half-period in x and y. The structure shown in this panel is persistent at late times.

real corona, direct ohmic dissipation of the equilibrium current sheet is negligible. Significant plasma heating occurs only when the instability produces steep gradients in the magnetic and velocity fields. In contrast, our numerical model has nonnegligible dissipation of the current sheet, even in the absence of the instability. By using the perturbed magnetic field to compute the current in equation (10b), we attempt to isolate the heating that is due to the instability alone. Note that all numerical simulations face the problem of unrealistically small Lundquist numbers. Finite numerical resolution produces a small effective Lundquist

number, even when the explicit number used in the MHD equations is large.

Figure 8 shows the ohmic and viscous heating rates as a function of time for the strong-shear case $C = 1.0$. The profiles are sharply peaked, with a FWHM of approximately $200\tau_A$. We determine the total energy dissipated by integrating over the duration of the event, t_f:
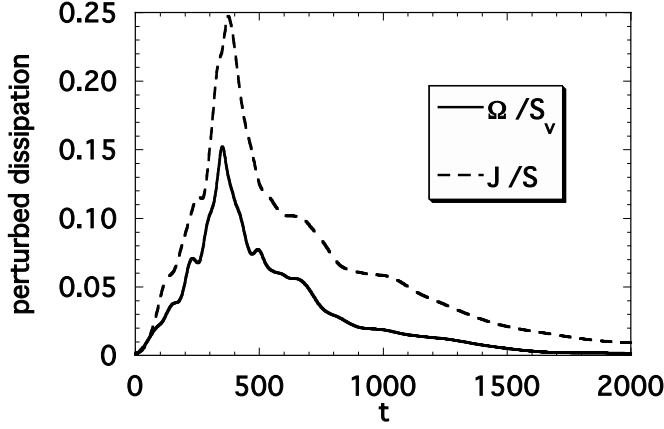
$$E_d = \int_0^{t_f} Q \, dt. \tag{14}$$

FIG. 8.—Ohmic dissipation (J/S) and viscous dissipation (Ω/S) vs. time for $C = 1.0$ and $S = S_v = 1000$.
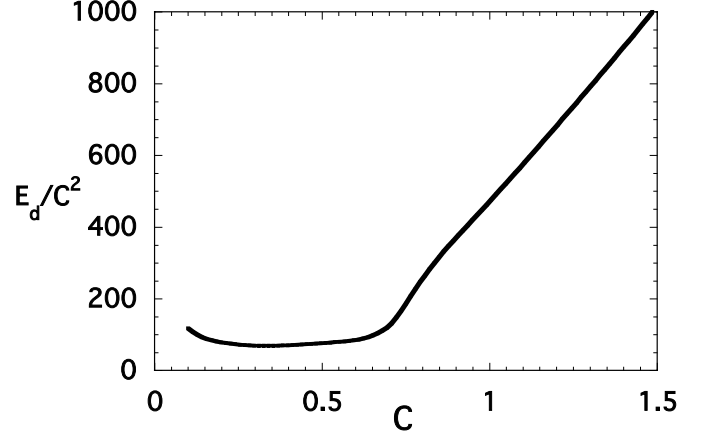

FIG. 9.—Total dissipated energy vs. C for $S = S_v = 1000$. The energy has been normalized by C^2, the free magnetic energy available in the equilibrium configuration.

Table 2 gives the results for simulations with shear parameters ranging from $C = 0.1$ to 1.5, using $t_f = 2223$. The energy increases monotonically with shear but jumps most significantly between $C = 0.7$ and 0.8, i.e., at a shear angle of about $70°$.

Since the magnitude of the guide field B_{0y} is the same in all simulations, the configurations with larger shear have greater magnetic energy. In particular, the free energy available for plasma heating depends on B_{0x}^2 and therefore scales as C^2. To better evaluate the dependence of heating on shear, we have normalized E_d by C^2 in the third column of Table 2. These values are also plotted as a function of C in Figure 9. We see that the normalized energy remains fairly constant up to $C = 0.7$. This heating is due mostly to the primary instability and is likely to be exaggerated in our simulations because of the small Lundquist numbers. The dramatic increase in normalized energy for $C > 0.7$ is clearly associated with the secondary instability. We note that this is somewhat larger than the threshold for linear instability ($C > 0.4$).

5. INTERPRETATION

We can interpret the secondary instability as a nearly ideal kinking of the twisted flux tubes that form from the primary instability. When C is small, the tubes have minimal twist because the ratio of shear-to-guide field (B_{0x}/B_{0y}) is small in the initial equilibrium. The ratio increases with increasing C, and so, too, does the twist of the tubes. Since the kink instability occurs only when a critical twist is exceeded (e.g., Linton et al. 1996, 1998), we have a natural explanation for why the secondary instability has a threshold in C.

TABLE 2
E_d AS A FUNCTION OF C

C	E_d	E_d/C^2
0.1	1.18	118
0.2	3.00	75
0.3	6.15	68
0.4	11.24	70
0.5	19.02	76
0.6	30.22	84
0.7	46.21	94
0.8	171.88	269
1.0	470.90	471
1.5	2283.6	1015

The well-known condition for flux tube kinking is that the helical field lines execute one complete turn over the wavelength of the unstable mode. From geometric considerations, we can express this condition as

$$2\pi r \frac{B_y}{B_x} \approx \lambda_y = \frac{2\pi}{k_y}, \tag{15}$$

where r is the characteristic radius of the tube. Flux tubes formed from the primary instability are not perfectly cylindrical but rather are flattened such that the cross section is wider along the current sheet than across it. From Dahlburg et al. (1992, Fig. 4), we take the characteristic radius to be

$$r \approx \frac{\lambda_x}{4} = \frac{\pi}{2k_x}. \tag{16}$$

Combining equations (15) and (16), noting that $k_x = k_y$ ($\alpha = \beta$), and taking $B_x/B_y = B_{0x}/B_{0y} = C$, we have

$$C_{\mathrm{crit}} \approx \frac{\pi}{2} \tag{17}$$

for the critical shear. Although this is roughly twice as large as the value we found from our nonlinear simulations, the agreement is quite good, given the gross assumptions that were made in deriving the result.

We can gain additional information about the secondary instability by performing a classical energy analysis (Bernstein et al. 1958), in which we calculate the sign of the potential energy δW of the system:

$$\frac{1}{4\pi} \int \left\{ |\nabla \times (\boldsymbol{v}_{3\mathrm{D}} \times \boldsymbol{B}_0)|^2 \right.$$
$$\left. - (\boldsymbol{v}_{3\mathrm{D}} \times \nabla \times \boldsymbol{B}_0) \cdot [\nabla \times (\boldsymbol{v}_{3\mathrm{D}} \times \boldsymbol{B}_0)] \right\} d^3x. \tag{18}$$

Here we have replaced the displacement with the velocity, which should not affect the sign of δW. Note that the surface terms drop out as a result of our boundary conditions. If δW is less than zero, the system is unstable. Figure 10 illustrates, for this run, the steps in the secondary instability process outlined in § 1. The three-dimensional mode grows at the primary instability rate ($\omega_i \sim 0.015$; see Fig. 5) before the two-dimensional mode saturates at
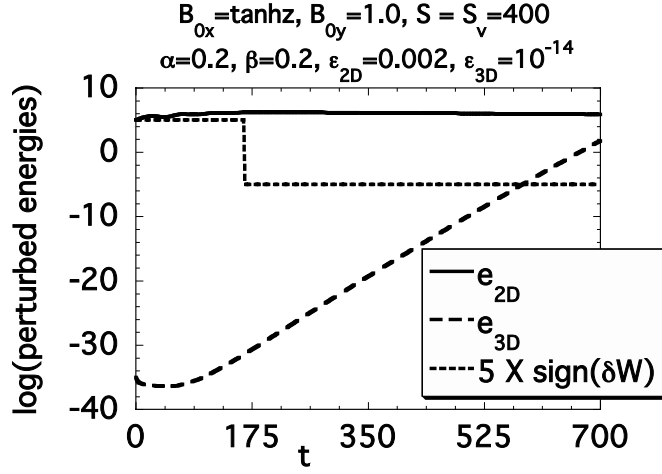
FIG. 10.—Perturbed energies and $5[\text{sign}(\delta W)]$ for $C = 1.0$.

FIG. 11.—One-dimensional to three-dimensional energy transfer terms vs. time for $C = 0.3$ and 0.4.

about $t \sim 50$. After saturation of the two-dimensional mode, however, the secondary instability is triggered, and this three-dimensional mode grows at a much faster rate, ~ 0.09. Although we have not investigated this aspect, we expect that the gap between the three-dimensional primary and secondary growth rates broadens with increasing Reynolds number because the primary mode becomes increasingly damped, while the secondary mode growth rate remains nearly constant, as seen already in analyses of the simpler component systems (e.g., Metcalfe et al. 1987; Dahlburg et al. 1992). Note also that our computations indicate that our chosen initial disturbance gives an initial positive value of δW. However, shortly after growth is observed in the three-dimensional energy, δW changes sign and becomes negative, indicative of an ideal instability.

To determine the efficiency and energetics of the secondary instability, we break down the time derivative of total energy into the energy transfer rates among all possible three-dimensional modes plus dissipative losses:

$$\frac{dE_3}{dt} = \tau_{13} + \tau_{23} + \delta_3, \qquad (19)$$

where $E_3 = \frac{1}{2}\langle |\boldsymbol{B}^{[3]}|^2 + |\boldsymbol{v}^{[3]}|^2 \rangle$ represents the magnetic and kinetic energy in the three-dimensional fields, τ_{13} represents the exchange of energy between one-dimensional and three-dimensional fields, τ_{23} represents the exchange of energy between two-dimensional and three-dimensional fields, and δ_3 represents the resistive and viscous diffusion of the three-dimensional fields. These terms are evaluated fully in Dahlburg (1997).

Hence, the normalized rate for energy transfer to and from the three-dimensional mode is

$$\Gamma \equiv \frac{1}{2E_3}\frac{dE_3}{dt} = \frac{\tau_{13}}{2E_3} + \frac{\tau_{23}}{2E_3} + \frac{\delta_3}{2E_3} = T_{13} + T_{23} + D_3. \qquad (20)$$

In previous work on a related problem in which the sheared magnetic field was held fixed while the guide magnetic field magnitude was varied (Dahlburg 1997), we have shown that changing the relative magnitude of the fieldwise and sheet-wise magnetic field components has a large effect on T_{13} and a much smaller effect on T_{23} and D_3. That is also the case here. In Figure 11 we show T_{13} as a function of time for cases with $C = 0.3$ and 0.4 for the same situation as shown in Figure 2. These values of the shear parameter (C) bracket the instability
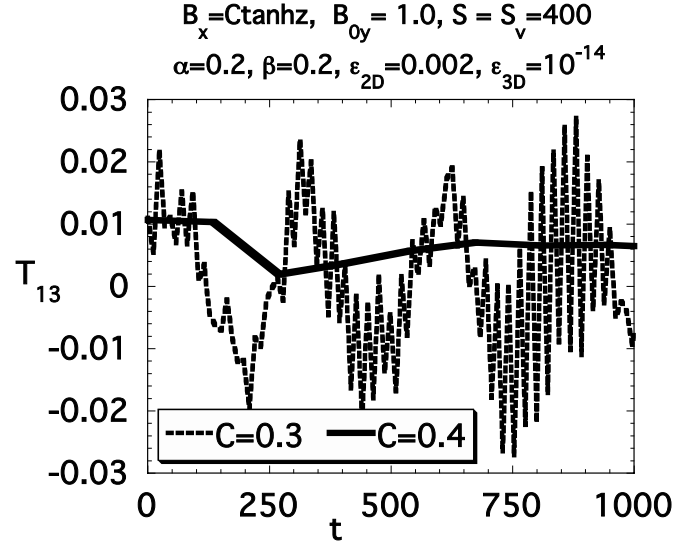
threshold, i.e., for $C = 0.3$ the secondary instability does not occur, whereas for $C = 0.4$ the secondary instability does occur. For both values of C there is an initial phase during which T_{13} is noisy, indicating that the three-dimensional instability has not yet emerged. Later, for $C = 0.3$ we see that T_{13} wanders around zero, whereas for $C = 0.4$ the term T_{13} remains positive, indicating a net transfer of energy from the one-dimensional to the three-dimensional fields. Hence, it appears that the T_{13} term is crucial in secondary instability energy transfer.

6. CURRENT SHEETS

In order to apply our results to the Sun, we must convert the dimensionless variables of our simulations into the corresponding physical quantities. Most of the normalization factors involved in this conversion, including the coronal magnetic field strength and coronal Alfvén speed, are well known from observations, but the thickness of a current sheet is not. We here estimate a thickness based on the coronal heating picture of Parker (1994) and Priest et al. (2002). Our estimate may not apply to other situations, such as flares and coronal mass ejections, in which the current sheet thickness could be much different.

Although our understanding of the photospheric magnetic field is still evolving, there is a general consensus that much of the flux is contained within small concentrations of intense field, often referred to as "kilogauss" (kG) flux tubes (e.g., Solanki 1993; Muller 1994). These concentrations may not be as tubelike as once thought (Berger & Title 1996), but such a description is a reasonable approximation for our purposes here. The flux tubes flare out dramatically in the chromosphere and transition region, and if there were no surrounding flux, they would come into contact with their neighbors at very low heights in the corona. Any relative motion of the footpoints, as produced by photospheric convection, for example, would then generate extremely thin current sheets at the coronal interfaces. In reality, appreciable flux does exist between the kG tubes (e.g., Meunier et al. 1998; Stenflo et al. 1998; Lin & Rimmele 1999), and it plays a major role in determining the thickness of the coronal current sheets. We refer to this flux as "weak flux" because its field strength in the photosphere is considerably less than that of the kG tubes. In the corona, where the plasma β is
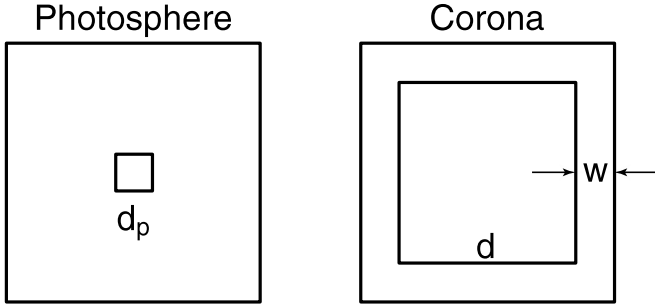
FIG. 12.—Photospheric (*left*) and coronal (*right*) cuts across an idealized kG flux tube and the surrounding weak flux. The dimension of the tube cross section increases from d_p in the photosphere to d in the corona.

small, the field strengths of the tubes and surrounding flux must be approximately equal in order to have lateral force balance.

To estimate the effect of the weak flux, imagine that the solar surface is partitioned into pieces, each associated with a single kG flux tube that lies at its center. For simplicity, we assume that the pieces and the flux tube cross sections have square shapes, as shown in Figure 12. The drawing on the left shows a layer in the photosphere, and the drawing on the right shows an overlying layer in the corona, above which the tube has flared out. Let the transverse size of the tube be designated by d_p in the photosphere and d in the corona. From flux conservation,

$$B_p d_p^2 = B d^2, \qquad (21)$$

where B_p and B are the magnetic field strengths of the tube in the photosphere and corona, respectively. Because the coronal field strength is approximately the same inside and outside the tube, the fraction of the total flux that is contained in the tube is roughly equal to the tube's fractional area in the corona:

$$f = \frac{d^2}{(d + 2w)^2}, \qquad (22)$$

where w is the half-width of the lane of weak flux that surrounds the tube (one-half the tube separation). Combining equations (21) and (22) gives

$$w = \frac{1}{2}\left(f^{-1/2} - 1\right)\left(\frac{B_p}{B}\right)^{1/2} d_p. \qquad (23)$$

Photospheric observations indicate that $B_p \approx 1500$ G, $d_p \approx 200$ km, and $f \approx 0.5$ (e.g., Solanki 1993; Meunier et al. 1998). It is possible that many flux tubes have a smaller diameter. Taking $B = 30$ G for an average coronal field strength in active regions (Mandrini et al. 2000), we have that $w \approx 300$ km or less.

The relationship between w and the current sheet half-width l depends on a number of factors, but especially on the pattern of mass flows in the photosphere. If the flows have a scale comparable to the flux tube separation, then the current sheet will occupy the entire volume between the tubes, and $l \approx w$. If the flows instead have narrow regions of extreme shear, like the faults of an earthquake, the current sheet will be much thinner than w. Another contributing factor is the shape of the flux tube cross section. Our idealized picture of square cross sections maximizes the tube separation. Tubes with circular cross sections, which are more likely if the tubes are twisted (Klimchuk et al. 2000), would have a distance of closest approach that is considerably less than w, as indicated in Figure 13. Small
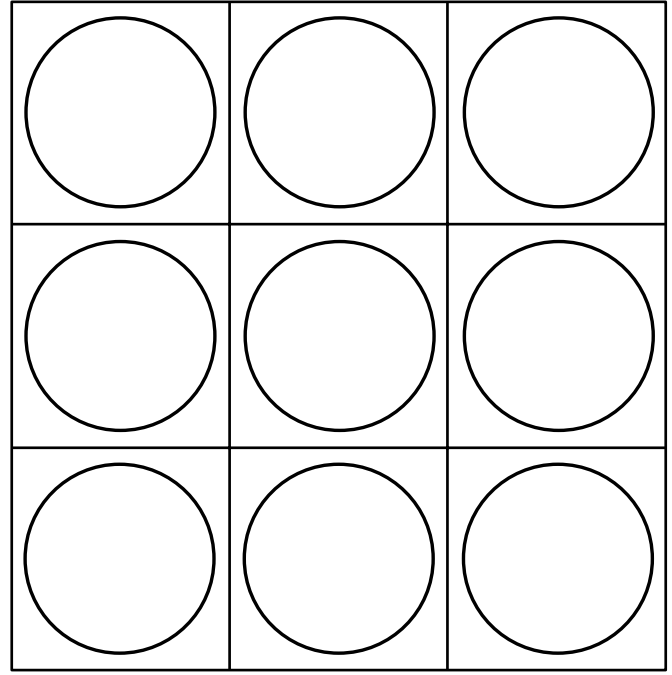

FIG. 13.—Coronal cut across an idealized array of nine circular cross section flux tubes.

separations are also expected if the tubes are wrapped around each other, since magnetic tension would act to pull the tubes together and push the intervening weak flux out of the way. All things considered, it seems reasonable to assume that the typical half-width of coronal current sheets is less than and perhaps much less than 100 km.

We note in passing that the choice $\alpha = 0.2$ places an upper limit on the ratio l/w. The current sheet dimension in the x-direction must obviously be smaller than the flux tube diameter d, and therefore, the x-dimension of our numerical box must also be smaller than d. In physical units, $L_x = 2\pi l/\alpha \approx 31.4l < d$. For $f = 0.5$, equation (22) gives $d = 4.8w$, and therefore $l/w < 0.15$. This seems reasonable based on the discussion above.

7. IMPLICATIONS FOR CORONAL HEATING

We are now ready to evaluate whether the secondary instability is a viable mechanism for coronal heating. As discussed in § 1, there are three basic requirements that must be satisfied: (1) the instability must remain dormant until the magnetic field has become sufficiently stressed; (2) it must proceed rapidly (at least as rapidly as the energy buildup rate) once it switches on; and (3) it must convert a sufficiently large fraction of the stored magnetic energy. We have already shown that the first requirement is satisfied. The secondary instability has a critical shear angle that agrees well with the angle inferred from observations. Both angles are of order a few tens of degrees, which is quite impressive given that either angle could have been within a small fraction of a degree of $0°$ or $180°$.

To address the second requirement, we adopt a typical coronal Alfvén speed $V_A = 1000$ km s^{-1} and current sheet half-width $l = 100$ km. The Alfvén transit time is then $\tau_A = 0.1$ s. With these units, we see from Figures 2, 3, and 8 that the secondary instability has a linear growth time of order 1 s and a nonlinear energy dissipation growth time of order 20 s. In comparison, the coronal field is stressed on a timescale given by $L/V_p = 10^5$ s, where $L = 10^5$ km is a typical coronal loop

length and $V_p = 1.0$ km s^{-1} is a typical photospheric velocity. The secondary instability therefore easily satisfies the requirement of being rapid. The growth rate of the primary instability is also very important, but we defer discussion of it until later.

Regarding the third requirement, we note from Table 2 and Figure 8 that the total energy dissipated during a heating event has a dimensionless value of roughly 200. To convert to physical energy, we multiply by $B^2 l^3/8\pi$. Taking $B = 30$ G and $l = 100$ km, we obtain $E_d = 7 \times 10^{24}$ ergs. This is a substantial energy release. It exceeds the canonical nanoflare energy of 3×10^{23} ergs first suggested by Parker (1994, p. 357), although both values are highly approximate.

In order for events of this magnitude to explain the heating of the corona, they must occur with a sufficient spatial density and temporal frequency. From Figure 13 we estimate that there are somewhat less than $2/d^2$ current sheets per unit area across the solar surface, where d is the coronal diameter of a kG flux tube. Each of these current sheets can support roughly L/L_y heating events along its length, where L is a typical coronal loop half-length and $L_y = 2\pi l/\beta$ is the y-dimension of our numerical box. If the events recur with a characteristic time interval Δt at each location, the flux of energy losses that could be powered by the events is given by

$$F = \frac{\beta}{\pi} \frac{L}{l} \frac{B}{B_p} \frac{E_d}{d_p^2 \Delta t}, \qquad (24)$$

where we have made use of equation (21). Using previously adopted values for L, l, B, and B_p and taking $d_p = 200$ km, we find that the observed energy flux from active regions, $F = 10^7$ ergs cm^{-2} s^{-1} (Withbroe & Noyes 1977), can be explained with an event recurrence interval of $\Delta t \approx 2000$ s. This interval seems quite plausible. It is both longer than the typical event duration (100 s) and shorter than the magnetic field stressing time (10^5 s).

How heating events recur at a particular location is something that we plan to explore in depth in a future study. It requires that "processed" magnetic flux from one event move aside so that new flux can "load up" the current sheet for the next event. Such behavior is not possible in the doubly periodic geometry of our present calculations. However, in the fully three-dimensional geometry of a finite current sheet, processed flux will naturally be expelled from the sheet (in the direction of the vertices in Fig. 13) because of the magnetic tension in the reconnected field lines. Whether a series of distinct heating events occurs or whether the instability develops into a quasi-steady Petschek-like reconnection remains to be determined.

We now return to the issue of the primary instability growth rate. As we have emphasized, the secondary instability begins only after the primary instability has modified the current sheet equilibrium. To explain coronal heating, the growth time of the primary instability must be shorter than the stressing time of the magnetic field. Because the primary instability is resistive, its dimensionless growth time increases with the Lundquist number, approximately as $S^{0.9}/4$. For a classical diffusivity of $\eta = 1.0 \times 10^{-6}$ km^2 s^{-1} (Priest 1982, p. 79), $S = V_A l/\eta \sim 10^{11}$, and the growth time is an extremely long 2×10^9 s. Thinner current sheets would have shorter growth times, but it is clear that in order for this mechanism to have relevance for the Sun, the diffusivity must be greatly enhanced compared to its classical value.

The secondary instability is not unusual in this regard. Most theories of coronal heating require anomalously large transport coefficients. This includes the popular ideas of steady reconnection (Parker 1973; Biskamp 1993, § 6.2.2; Priest & Forbes 2000, § 5.4.) and wave heating by resonance absorption (Ofman et al. 1994). Recent observations provide compelling evidence that transport coefficients are indeed greatly enhanced. Nakariakov et al. (1999) studied transverse loop oscillations observed by *TRACE* and concluded that the rapid damping requires an effective Lundquist number of $S = 10^6$ (although see the concerns raised by Solovév et al. [2002]). Using this value, the growth time of the primary instability is only 6×10^4 s, less than the magnetic field stressing time.

8. FINAL REMARKS

Our results suggest that the secondary instability is a very promising explanation of coronal magnetic energy release, especially in the context of coronal heating. As far as we are aware, it is the only mechanism so far proposed that has the necessary switch-on property. This is a fundamental property that, in our view, has been greatly underappreciated. It is required to explain a whole host of coronal phenomena, not only coronal heating.

While we are very encouraged by our initial results, much more work needs to be done before the secondary instability is established as playing a central role in coronal energy release. On the theoretical side, we must relax some of the assumptions that restrict our current simulations. First, we need to examine the consequences of finite current sheet dimensions. Our infinite current sheet geometry prevents us from studying the "reloading" of the current sheet that is required for multiple events, and it eliminates line-tying effects that could potentially be important. Second, we need to investigate time-dependent shearing. We have thus far assumed a background field that is constant in each simulation. This is reasonable once the highly explosive secondary instability begins, but it may not be appropriate for the much slower primary instability. We have emphasized that the primary instability creates a modified equilibrium in which the secondary instability can occur. The properties of this equilibrium will be different if the shear of the background field changes as the primary instability grows. This is likely to influence the secondary instability. For example, the narrow flux tubes that are created by the resistive tearing of the current sheet will have different twist profiles, $\phi(r)$, with the outer "shells" of the tubes being more highly twisted than the inner cores. It is known that the properties of the kink instability depend on the details of the twist profile (e.g., Lionello et al. 1998). Some profiles produce a global kinking of the tube, while others produce an internal rearrangement of the field, leaving the global structure essentially unchanged. How this may affect the secondary instability is an open question.

We also need to determine whether the response of the coronal plasma to secondary instability heating is consistent with soft X-ray and EUV observations. This effort will likely involve one-dimensional hydrodynamic loop modeling, at least initially. Evidence is mounting that many observed coronal loops cannot be explained by steady heating (e.g., Aschwanden et al. 2001; Winebarger et al. 2003; Patsourakos et al. 2004) and that impulsive heating by nanoflares is a much more viable explanation (e.g., Cargill & Klimchuk 1997; Klimchuk 2002; Warren et al. 2003). We plan to use the heating predicted by our MHD simulations as input to detailed loop hydromodels. We will then synthesize the emission from the models and compare it with loop observations from current (*Yohkoh*, *SOHO*, and *TRACE*) and future (*Solar-B* and the *Solar Dynamics Observatory*) missions.

Finally, the properties of coronal current sheets are poorly determined at this time. As discussed in § 6, these properties depend critically on the weak flux that surrounds kG flux tubes. The nature of this weak flux (e.g., whether and how it is fragmented and sheared in the photosphere) is itself highly uncertain. Even the parameter *f* that describes the partitioning of the total coronal flux between kG tubes and the surrounding flux is known only approximately. This situation should change dramatically when *Solar-B* is launched and the visible-light telescope obtains images and magnetograms of unprecedented quality. We anxiously await these results and will modify our simulation parameters accordingly.

REFERENCES

Aschwanden, M. J., Schrijver, C. J., & Alexander, D. 2001, ApJ, 550, 1036
Berger, T. E., & Title, A. M. 1996, ApJ, 463, 365
Bernstein, I. B., Frieman, E. A., Kruskal, M. D., & Kulsrud, R. M. 1958, Proc. R. Soc. London A, 244, 17
Biskamp, D. 1993, Nonlinear Magnetohydrodynamics (Cambridge: Cambridge Univ. Press)
Cargill, P. J., & Klimchuk, J. A. 1997, ApJ, 478, 799
Dahlburg, R. B. 1994, Phys. Plasmas, 1, 3053
———. 1997, J. Plasma Phys., 97, 35
———. 1998, Phys. Plasmas, 5, 133
Dahlburg, R. B., Antiochos, S. K., & Klimchuk, J. A. 2003, Adv. Space Res., 32, 1029
Dahlburg, R. B., Antiochos, S. K., & Zang, T. A. 1992, Phys. Fluids B, 4, 3902
Dahlburg, R. B., & Einaudi, G. 2001, Phys. Plasmas, 8, 2700
———. 2002, Phys. Lett. A, 294, 101
Dahlburg, R. B., & Karpen, J. T. 1995, J. Geophys. Res., 100, 23489
Dahlburg, R. B., Montgomery, D., & Zang, T. A. 1986, J. Fluid Mech., 169, 71
Dahlburg, R. B., Montgomery, D., Zang, T. A., & Hussaini, Y. 1983, Proc. Natl. Acad. Sci., 80, 5789
Forbes, T. 2000, J. Geophys. Res., 105, 23153
Horiuchi, R., & Sato, T. 1986, Phys. Fluids, 29, 1161
Klimchuk, J. A. 2001, in Space Weather, ed. P. Song, H. Singer, & G. Siscoe (Geophys. Monogr. 125; Washington: AGU), 143
———. 2002, in Solar Magnetism and Related Astrophysics, ed. G. Fisher & D. Longcope (Santa Barbara: Univ. California), http://online.kitp.ucsb.edu/online/solar_c02/klimchuk
Klimchuk, J. A., Antiochos, S. K., & Norton, D. 2000, ApJ, 542, 504
Lin, H., & Rimmele, T. 1999, ApJ, 514, 448
Linton, M. G., Dahlburg, R. B., Fisher, G., & Longcope, D. W. 1998, ApJ, 507, 404
Linton, M. G., Longcope, D. W., & Fisher, G. 1996, ApJ, 469, 954

Lionello, R., Velli, M., Einaudi, G., & Mikić, Z. 1998, ApJ, 494, 840
Mandrini, C. H., Démoulin, P., & Klimchuk, J. A. 2000, ApJ, 530, 999
Metcalfe, R., Orszag, S. A., Brachet, M. E., Menon, S., & Riley, J. J. 1987, J. Fluid Mech., 184, 207
Meunier, N., Solanki, S. K., & Livingston, W. W. 1998, A&A, 331, 771
Muller, R. 1994, in Solar Surface Magnetism, ed. R. J. Rutten & C. J. Schrijver (Dordrecht: Kluwer), 55
Nakariakov, V. M., Ofman, L., DeLuca, E., Roberts, B., & Davila, J. M. 1999, Science, 285, 862
Ofman, L., Davila, J. M., & Steinolfson, R. S. 1994, ApJ, 421, 360
Parker, E. N. 1973, J. Plasma Phys., 9, 49
———. 1983a, ApJ, 264, 635
———. 1983b, ApJ, 264, 642
———. 1988, ApJ, 330, 474
———. 1994, Spontaneous Current Sheets in Magnetic Fields (New York: Oxford Univ. Press)
Patsourakos, S., Klimchuk, J. A., & MacNeice, P. J. 2004, ApJ, 603, 322
Priest, E. R. 1982, Solar Magnetohydrodynamics (Dordrecht: Reidel)
Priest, E. R., & Forbes, T. 2000, Magnetic Reconnection: MHD Theory and Applications (Cambridge: Cambridge Univ. Press)
Priest, E. R., Heyvaerts, J., & Title, A. M. 2002, ApJ, 576, 533
Schumacher, J., & Seehafer, N. 2000, Phys. Rev. E, 61, 2695
Seehafer, N., & Schumacher, J. 1998, Phys. Plasmas, 5, 2363
Solanki, S. K. 1993, Space Sci. Rev., 63, 1
Solovév, A. A., Mikhalyaev, B. B., & Kiritchek, E. A. 2002, Plasma Phys. Rep., 28, 758
Stenflo, J. O., Keller, C. K., & Gandorfer, A. 1998, A&A, 329, 319
Warren, H. P., Winebarger, A. R., & Mariska, J. T. 2003, ApJ, 593, 1174
Winebarger, A. R., Warren, H. P., & Mariska, J. T. 2003, ApJ, 587, 439
Withbroe, G. L., & Noyes, R. W. 1977, ARA&A, 15, 363